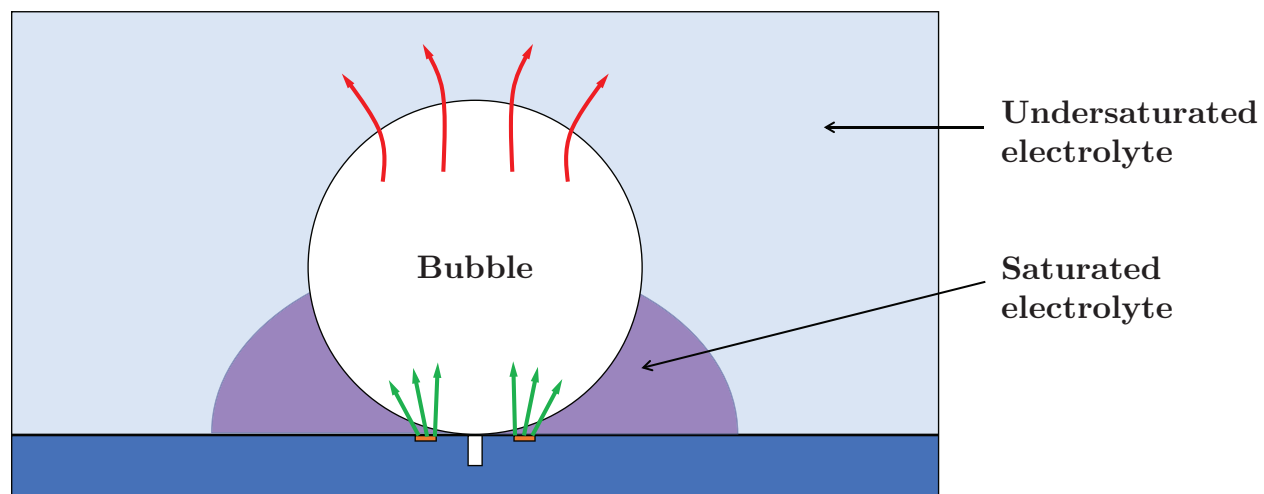# Graphical Abstract

Investigating Mass Transfer Around Spatially-Decoupled Electrolytic Bubbles

Akash Raman, Carla Corina dos Santos Porto, Han Gardeniers, Cíntia Soares, David Fernández Rivas, Natan Padoin

Investigating Mass Transfer Around Spatially-Decoupled Electrolytic Bubbles

Akash Raman[a,*], Carla Corina dos Santos Porto[b], Han Gardeniers[a], Cíntia Soares[b,*], David Fernández Rivas[a], Natan Padoin[b]

[a]*Mesoscale Chemical Systems Group, MESA+ Institute for Nanotechnology, Faculty of Science and Technology, University of Twente, P.O. Box 217, Enschede, 7500 AE, The Netherlands*
[b]*Laboratory of Materials and Scientific Computing - LabMAC, School of Technology, Federal University of Santa Catarina (UFSC), 88040-900, Florianópolis/SC, Brazil*

Abstract

Electrolytic bubbles have a profound impact on mass transport in the vicinity of electrodes, greatly influencing the electrolyzer efficiency and cell overpotential. However, high spatio-temporal resolution experimental measurements of concentration fields around electrolytic bubbles, are challenging. In this study, a succession of spatially-decoupled electrolytic bubbles are simulated. The bubbles grow, and departing from a hydrophobic cavity at the center of a ring microelectrode. The gas-liquid interface is modeled using a moving mesh topology. A geometric cutting protocol is developed to handle topology changes during bubble departure. The simulated bubbles show good agreement with the bubble growth dynamics observed in experiments. The bubbles in this spatially-decoupled system outgrow the region of electrolyte that is saturated with dissolved hydrogen. This leaves the apex of the bubble interfaces exposed to an undersaturated region of the electrolyte which leads to an outward flux of hydrogen gas. This is shown to limit the gas evolution efficiency of bubbles despite the fact that they grow at a constant volumetric rate. By analyzing the distribution of the flux of dissolved hydrogen along the bubble interface along with the development of dissolve hydrogen concentration profiles around the bubble, we show that the magnitude of the outward diffusive flux at the apex of the bubble decreases with increasing electrolysis

---

*Corresponding author.
Email addresses: `a.raman@utwente.nl` (Akash Raman), `cintia.soares@ufsc.br` (Cíntia Soares)

current.

Keywords: hydrogen, water electrolysis, electrolytic bubbles, mass transfer, direct numerical simulation, moving mesh

1. Introduction

The decarbonization of industries is a key step in reaching net-zero carbon emissions and low-carbon hydrogen is expected to play a key role in this transition [1]. Water electrolysis offers a robust way to generate clean hydrogen for industrial, and commercial applications while also raising the possibility of offsetting the intermittency of renewable energy sources [2, 3]. As a result, water electrolysis driven by renewable energy sources is expected to meet $\sim 38\%$ of global hydrogen demand by 2030 [4].

Gas bubbles nucleate on the surface of electrodes during gas-evolving electrochemical reactions such as water electrolysis. These electrolytic bubbles are known to greatly influence the transport of dissolved product gases, as well as the transport of ionic species, in the vicinity of the electrode [5]. Electrolytic bubbles are a significant source of inefficiency in electrolyzers. They increase the electrical resistance in electrolyzers by restricting ion conduction pathways in the electrolyte, and by covering portions of the electrode and rendering them inactive [5–10]. However, bubbles can also lower the concentration of dissolved gases, and induce microconvective flows - effects known to have a positive influence on electrolysis [11–16]. It has been suggested that the optimization of bubble evolution phenomena can lead to a 5-10 % improvement in electrolysis stack efficiency [17]. Therefore, advancing our understanding of electrolytic bubbles is important in the context of global climate change mitigation.

Several publications on the topic have focused on studying the nucleation, growth and departure dynamics of electrolytic bubbles under varying conditions [14, 15, 18–32]. However, the design of next-generation electrodes with optimized bubble evolution characteristics requires greater understanding of the evolution of the concentration profile of dissolved gas in the vicinity of the bubbles. Advances in high speed imaging techniques, and confocal

microscopy have opened up possibilities to observe bubble-related phenomena with much greater spatio-temporal resolution than before [33]. Scanning probe techniques such as scanning electrochemical microscopy (SECM) have been used to measure local dissolved gas concentrations in the vicinity of bubbles [34–37]. However, the presence of the SECM probe, and its movement during raster scans can influence the concentration profile and disrupt natural convective flows. Recent studies have applied confocal fluorescence microscopy to study variations in pH around electrolytic bubbles [38, 39]. The development of new fluorescent probes for fluorescence lifetime imaging microscopy also open up new possibilities in this direction [40]. Nevertheless, the direct experimental measurement of the concentration gradients in three dimensions surrounding electrolytic bubbles remains a challenge due to the presence of complex convective flows, and the fast growth of the bubbles in comparison to the timescales required by analytical techniques. Several studies have attempted to fill this gap in knowledge through the use of direct numerical simulations (DNS) which can offer the necessary spatio-temporal resolution required to understand electrolytic bubble evolution across length scales.

Vachaparambil and Einarsrud [41] simulated the growth of a rising bubble in a supersaturated medium using the volume of fluid (VOF) model. The compressive continuous species transfer model, the sharp surface force model, the driving force for the bubble growth (Fick's first law and a mass transfer correlation), as well as the relevant source terms, were implemented in the open source code OpenFOAM 6. The authors validated their numerical predictions against theoretical models (Epstein–Plesset, Scriven, and Extended Scriven).

This VOF-based framework was further extended by the respective authors to account for single, and dual bubble growth, and departure, considering coalescence in the latter case [42]. The authors considered a coupling of multiphase flow, electrochemical reactions, species and charge transport, and interfacial mass transfer in their simulations. The model was verified with analytical models for bubble growth in supersaturated medium, steady bubble, and rising bubble.

4

Other studies have used the VOF method to simulate interface-resolved growth, and in some cases departure and rise, of electrolytic bubbles [43, 44]. However, different alternatives are available for multiphase modeling, as highlighted by Taqieddin et al. [45]. Of the interface capturing methods, phase-field [46, 47] and level-set [48, 49] are also relevant. While they are less precise than moving mesh in the computation of the fluxes across the interface, they allow topology changes - a significant advantage for simulating bubble departure from a surface.

Using a sharp interface immersed boundary method and artificial compressibility for the pressure, Khalighi et al. [51] studied the growth of a single hydrogen bubble attached to a vertical cathode in a narrow channel under forced convection conditions. The authors solved the Navier-Stokes equations, as well as the species balance and potential equations. The effect of the fluid flow rate and the operating pressure was evaluated, considering the bubble growth behavior, species concentration, potential, and current density as dependent variables. Although a rigorous numerical analysis was carried out, the results were not compared to experimental data or analytical models, and bubble departure was not considered.

Other studies have also considered the influence of variations in physical properties, e.g., density and surface tension, due to thermal and solutal gradients. Sepahi et al. [52] used the immersed boundary method to study the growth of single and multiple hydrogen bubbles in acidic water electrolysis and compared their theoretical predictions with experimental data. The authors found a significant effect of buoyancy-driven convection on the bubble dynamics. Moreover, investigations about Marangoni convection due to thermo-, and solutal-capillary effects have also been reported [53–55]. Using a finite element method-based solver, Meulenbroek et al. [54] investigated the formation of Marangoni forces that retarded the departure of electrolytic hydrogen bubbles. A stagnant cap formed by compression of surfactants at the apex of the bubble, suppressing motion in that portion, was considered in the simulations, either specifying a stagnation angle at the interface or calculating the dynamic formation of this region. However, a mobile interface was considered at the bottom of the bubble, where

5

Marangoni flow causes the formation of vortices.

Furthermore, several contributions on the simulation of multiple bubbles generated by hydrogen evolution from water electrolysis in larger electrodes using Euler-Euler and Euler-Lagrange formulations can also be found in literature [56–63]. Such approach do not consider the gas-liquid interface explicitly, but are well-suited for the investigation of the effect of electrolytic bubbles on the performance of electrolyzers on a macro-scale.

The vast majority of studies on electrolytic bubbles consider the formation of the bubbles directly atop the electrode surface. An exception to this is the study by Peñas et al. [14] which investigated the evolution of hydrogen bubbles from a hydrophobic microcavity away from a ring microelectrode surface, spatially decoupling the site of bubble nucleation from the site of water electrolysis. The study considered experiments, and a simplified numerical model that allowed a qualitative understanding of the effect of bubble evolution on the concentration, and Ohmic overpotential. A subsequent analysis of bubble growth, and its influence on the half-cell potential in this decoupled electrolysis system was performed with the aid of a simplified numerical model which calculated the change in Ohmic resistance in the system as a function of bubble radius [15]. This combination of experiments and modeling showed the precise influence of bubbles on the concentration overpotential. The bubble was considered a fixed domain, and bubble departure was not explicitly considered in the aforementioned studies considering spatially decoupled electrolysis.

In this paper, we present a detailed DNS investigation of convective, and diffusive mass transfer around single, successive, spatially-decoupled electrolytic bubbles growing in the superhydrophobic pit-ring system. The adoption of an arbitrary Lagrangian-Eulerian (ALE) moving mesh method allowed the detailed quantification of the fluxes at the bubble interface. Since the ALE moving mesh method cannot handle topology changes, an interface cutting protocol was developed to re-initialize the simulation during bubble departure. Herein, we simulate larger bubbles than the ones commonly reported in the literature, which grow beyond the concentration boundary layer. The time-dependent investigation considering
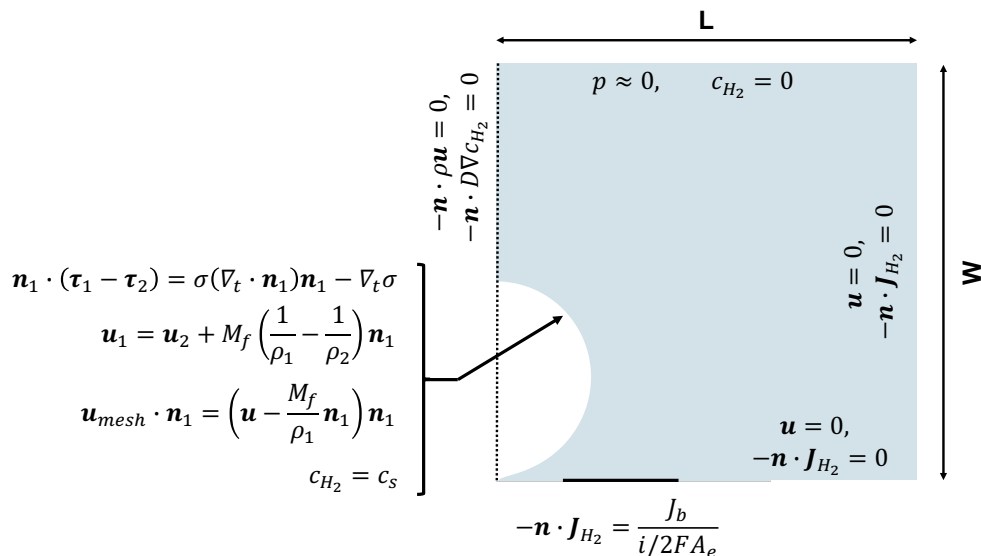
6

Figure 1: A schematic representation of the 2D axisymmetric model geometry. The bubble is depicted as a white semicircle. The boundary conditions specified in the geometry are indicated. The axis of symmetry is the left edge of the schematic indicated by the dotted line.

coupled fluid flow and mass transfer is presented, which represents a significant advancement regarding the study of Peñas et al. [14].

2. Numerical simulation setup and methodology

The numerical simulations were performed in a 2D axisymmetric domain with the finite element-based solver COMSOL® Multiphysics (Burlington MA, USA). The computational domain, highlighting the dimensions and the location of the boundary conditions, is depicted in detail in Fig. 1. The numerical model was designed to closely resemble the experimental system in which electrolytic bubbles nucleate, grow, and depart from a hydrophobic cavity or radius $r_p = 10$ μm surrounded by a ring electrode of inner radius $r_i = 230$ μm , and outer radius $r_o = 255$ μm. The computational geometry consists of a 7 mm × 7 mm rectangular domain. The incipient bubble was described as a quadrant of radius r_p centered at the geometric origin. The electrode was described as a line segment on the x-axis between $x = r_i$, and $x = r_o$.

Additional rectangular subdomains were defined in order to prescribe finer meshing pa-

7

rameters around the bubble, and around the electrode surface. First, a 2 mm × 1.2 mm rectangular subdomain was built starting from the origin to allow the discretization with a finer mesh in the region of the greatest mesh deformation during the bubble growth phase. In the bubble rise phase, the height of this rectangular subdomain was extended to the top of the geometry by creating a 7 mm × 1.2 mm rectangular subdomain. Second, a 45 μm × 10 μm rectangular subdomain was built around the electrode to ensure greater mesh refinement in order to better capture the steep concentration gradients in this region.

The entire domain was initially discretized with a non-structured mesh consisting of approximately $9{\times}10^4$ elements. A finer mesh was imposed also at the bubble interface throughout the entire simulations, ensuring a proper resolution independently of the bubble size. Moreover, a mesh refinement study was carried out to ensure that the final mesh produced independent results throughout the entire run. All initial meshing parameters are described in the supplementary information (see SI Sec. S1.1). Remeshing was needed throughout the simulation to ensure proper mesh refinement as the bubbles grow or rise. A maximum mesh distortion threshold (see SI Sec. S1.1), with backward Euler consistent initialization, was considered in all cases.

Pure water and hydrogen at room conditions were considered as the liquid and gas phases, respectively. The diffusivity of H_2 in water was fixed at $5{\times}10^{-9}$ m^2·s^{-1} in all simulations [64]. Since the currents considered in the study were ≤ 50 μA , no appreciable changes in the temperature of the electrolyte were expected. As a result, isothermal conditions were assumed in all cases, and the temperature was fixed as T = 300 K. The Henry's constant of H_2 , $k_H = = 7.7 \times 10^{-6}$ mol·m^{-3} was considered in all simulations [65]. The electrolyte was equilibriated with the atmosphere before, and during the experiments. Thus, a uniform initial concentration of $c_i = 3.85{\times}10^{-7}$ mol·m^{-3} (considering 0.5 ppm of H_2 in air [66]), and quiescent conditions ($\mathbf{u} = 0$) were specified throughout the electrolyte domain.

A time-dependent profile was specified for the H_2 concentration at the bubble interface for the first bubble. The concentration at the bubble-electrolyte boundary was increased
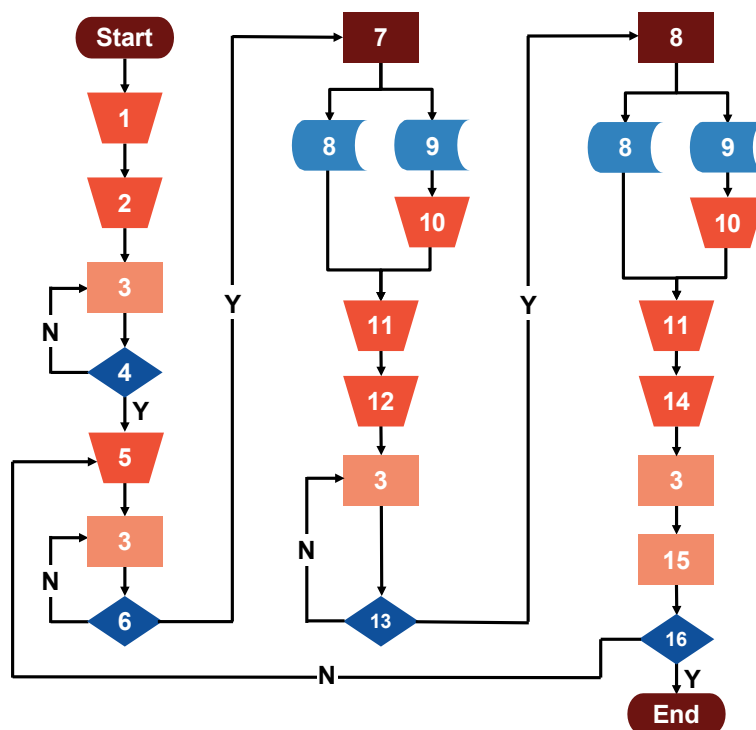
8

Figure 2: Numerical procedure flowchart. (1) Initialization of geometry, mesh, initial conditions, boundary conditions and remeshing parameters. (2) Setting up a time-dependent boundary condition at the bubble interface. (3) Solving mass, momentum, and species balance equations. (4) Checking if $t \geq t_s$ where t_s is the time taken for the electrolyte to become saturated at the bubble nucleation site with a stationary (non-growing) bubble. (5) Boundary condition at the bubble interface is a constant value of $c = c_s$ where c_s is the saturation concentration. (6) Checking if the bubble neck radius has reached the threshold, $r_{min} \leq 20$ nm. (7) Stopping the calculation. (8) Saving the current mesh. (9) Saving the flow variables (velocity components, pressure, and concentration). (10) Replacing voids by c_s. (11) Importing and interpolating the flow variables into a new simulation setup. (12) Enforcing bubble departure. (13) Checking if $z_{max,rising} < z_{threshold}$. (14) Removing the rising bubble. (15) Incrementing the bubble count (N). (16) Checking if $N > N_{total}$.

9

from c_i at the beginning of the simulation, to the saturation concentration of H$_2$, $c_s = 0.77$ mM at the saturation time t_s. The saturation time, t_s is the time taken for the saturation of the electrolyte layer immediately adjacent a stationary (non-growing) bubble interface at the hydrophobic cavity. The concentration profile, and t_s were approximated based on a preliminary simulation without the moving mesh topology. Thus, the preliminary simulation considered only diffusion of the hydrogen from at the ring electrode surface to the surface of a stationary bubble. Details of the preliminary simulation, and the concentration profiles used for the time-dependent boundary condition are presented in SI Sec. S1.3. The time-dependent ramp was necessary because the electrolyte surrounding the gas cavity is initially undersaturated, and a time-invariant boundary condition of $c = c_s$ would cause the bubble to shrink. Following the initial ramp, a constant concentration equal to c_s was maintained at the bubble interface for the remainder of the simulation. Furthermore, the time-dependent concentration boundary was not applied to subsequent bubbles which nucleate within a saturated region of the electrolyte.

The mathematical model consisted of a set of nonlinear partial differential equations describing the fluid flow and the H$_2$ transport within the computational domain. While the fluid flow equations were solved in all subdomains (liquid and gas), the H$_2$ transport equation was solved only in the liquid phase. Section 2.1 presents the details of the mathematical model solved herein. The balance equations (momentum and species transport) were solved with the direct MUltifrontal Massively Parallel Solver (MUMPS) [67, 68]. Moreover, the Backward Differentiation Formula (BDF) solver was used for calculating the time step [69].

In all models, the electrolysis current was specified as a constant flux of H$_2$ at the ring electrode's surface (see SI Sec. S1.2). The bubble grows due to H$_2$ transport across the interface, which was calculated by integrating the H$_2$ diffusive flux weighted by the molecular weight of H$_2$ along the bubble interface. The calculation was stopped when the neck radius r_{min}, which was measured as the minima of the radial coordinate along the bubble interface, falls below a threshold $r_{min} \leq 20$ nm.

10

Then, the mesh and the flow variables (velocity components, pressure, and concentration) were exported for the simulation of the departure of the bubble from the hydrophobic cavity, and its subsequent rise through the bulk of the electrolyte. The same initial meshing and remeshing parameters considered in the bubble growth step were adopted. Therefore, the flow variables were interpolated in the initial mesh generated for the bubble departure and rising step. However, since the species transport equations were not solved in the bubble domain, voids in the concentration matrices were replaced by the H_2 saturation concentration ($c_s = 7.7 \times 10^{-6}$ mol·m^{-3}) for consistency.

Moreover, since the implementation of the moving mesh model considered herein does not allow topological change, the departure event was implemented by altering the model geometry and splitting the single bubble domain into a rising bubble, and an incipient cap pinned to the hydrophobic cavity. The position of the bubble neck was identified as the minima of the radial coordinate along the bubble interface, and the region was cut by removing a 5 μm tall rectangular portion (see SI Sec. S1.4), resulting in a separation between the interface of the rising bubble and the interface of the bubble remaining at the pit.

The bubble rising event was simulated until the bubble interface reached a distance of 200 μm from the upper boundary of the computational domain. Then, the mesh and the data at the last time step were exported. A new simulation was initialized with the exported topology and variables. In the setup for the simulation of the second bubble growth, the bubble at the top of the computational domain was removed. The initial mesh and remeshing parameters were also the same mentioned earlier. Therefore, the imported flow variables (velocity components, pressure, and concentration) were interpolated throughout the elements of the current mesh, considering a replacement of the voids in the matrix by the H_2 saturation concentration ($c_s = 7.7 \times 10^{-6}$ mol·m^{-3}) for consistency.

The subsequent bubbles were simulated subject to the same parameters, and protocol described above. When the stop condition for the second bubble growth was reached (same for the first bubble, i.e., $r_{min} \leq 20$ nm), the departure and rising event were then simulated

11

according to the procedure described in the previous paragraphs. This setup was considered for the seven cycles simulated herein. Figure 2 presents a flow chart summarizing the procedure adopted in the numerical simulations.

2.1. Mathematical Model

2.1.1. Fluid Dynamics

The bubble growth and bubble rising events were calculated with the moving mesh Arbitrary Lagrangian–Eulerian (ALE) formulation [70–72].

The 2D axisymmetric, Newtonian, time-dependent, laminar and incompressible flow occurring in the device was modeled according to the momentum and overall mass balance equations represented by Eqs. 1 and 2, respectively:

$$\rho\frac{\partial \mathbf{u}}{\partial t} + \rho(\mathbf{u} \cdot \nabla)\mathbf{u} = \nabla \cdot [-p\mathbf{I} + \mu(\nabla\mathbf{u} + (\nabla\mathbf{u})^T)] + \rho\mathbf{g} \tag{1}$$

$$\nabla \cdot \mathbf{u} = 0 \tag{2}$$

where ρ (kg·m^{-3}) is the density, $\mathbf{u}$ (m·s^{-1}) is the velocity field, p (kg·m^{-1}·s^{-1}) is the pressure, μ (kg·m^{-1}·s^{-1}) is the dynamic viscosity, $\mathbf{I}$ (dimensionless) is the identity matrix, T (dimensionless) is the transpose operator and $\mathbf{g}$ (m·s^{-2}) is the gravity acceleration.

At the gas-liquid interface, the finite stresses were calculated according to Eq. 3.

$$\mathbf{n}_1 \cdot (\boldsymbol{\tau}_1 - \boldsymbol{\tau}_2) = \boldsymbol{f}_{st} \tag{3}$$

where $\boldsymbol{\tau}_1$ (N·m^{-2}) and $\boldsymbol{\tau}_2$ (N·m^{-2}) are the total stress tensors in each phase (gas and liquid, respectively) at the interface ($\boldsymbol{\tau}_i = -p\boldsymbol{I} + \mu_i(\nabla\boldsymbol{u}_i + (\nabla\boldsymbol{u}_i)^T)$), while $\boldsymbol{n}$ (dimensionless) is the normal to the interface. The term $\boldsymbol{f}_{st}$ (N·m^{-2}) corresponds to the force per unit area related to the surface tension, expressed in Eq. 4.

$$\boldsymbol{f}_{st} = \sigma(\nabla_t \cdot \boldsymbol{n}_1)\boldsymbol{n}_1 - \nabla_t\sigma \tag{4}$$

where σ is the surface tension coefficient (N·m^{-1}) and ∇_t is the surface gradient operator.

Moreover, continuity of the velocity field is considered at the interface, according to Eq. 5.

$$\boldsymbol{u}_1 = \boldsymbol{u}_2 + M_f \left(\frac{1}{\rho_1} - \frac{1}{\rho_2} \right) \boldsymbol{n}_1 \tag{5}$$

where $\boldsymbol{u}_1$ (m·s^{-1}) and $\boldsymbol{u}_2$ (m·s^{-1}) are the velocity of the gas and liquid phases, respectively, at the interface.

M_f (kg·m^{-2}·s^{-1}) is the interfacial H$_2$ mass flux given by Eq. 6.

$$M_f = (J_{H_{2,r}} \cdot n_{1,r} + J_{H_{2,z}} \cdot n_{1,z})MW_{H_2} \tag{6}$$

where $J_{H_{2,r}}$ and $J_{H_{2,z}}$ (kmol·m^{-2}·m^{-1}) are the diffusive flux of H$_2$ in the r and z directions, respectively, n_r and n_z are the r and z normal components at the gas-liquid interface, and MW_{H_2} (kg·kmol^{-1}) is the molecular weight of H$_2$.

Finally, the mesh velocity was calculated according to Eq. 7.

$$\boldsymbol{u}_{mesh} \cdot \boldsymbol{n}_1 = \left(\boldsymbol{u} - \frac{M_f}{\rho_1}\boldsymbol{n}_1 \right) \cdot \boldsymbol{n}_1 \tag{7}$$

No-slip conditions were considered at the walls. Moreover, null gauge pressure was applied at the top surface of the computational domain (open to the atmosphere).

2.1.2. Mass Transfer

The time-dependent convection-diffusion equation (Eq. 8) was used to model the transport of hydrogen in the liquid phase.

$$\frac{\partial c_{H_2}}{\partial t} + \nabla \cdot \boldsymbol{J}_{H_2} + \boldsymbol{u} \cdot \nabla c_{H_2} = 0 \tag{8}$$

13

where c_{H_2} (mol·m^{-3}) is the concentration of H$_2$ in the liquid phase, $\boldsymbol{J}_{H_2}$ (kmol·m^{-2}s^{-1}) is the diffusive flux of H$_2$ in the liquid phase and $\boldsymbol{u}$ (m·s^{-1}) is the velocity field.

The diffusive flux of H$_2$ in the liquid phase was modeled by Fick's first law, given by Eq. 9.

$$\boldsymbol{J}_{H_2} = -D\nabla c_{H_2} \tag{9}$$

where D (m^2·s^{-1}) is the H$_2$ diffusivity in the liquid phase.

H$_2$ impermeability ($-\boldsymbol{n}\cdot\boldsymbol{J}_{H_2} = 0$) was considered at the walls. A specified H$_2$ flux was imposed at the ring electrode's surface ($-\boldsymbol{n}\cdot\boldsymbol{J}_{H_2} = \boldsymbol{J}_{H_{2,0}}$). Moreover, the H$_2$ saturation concentration $c_s = 7.7\times10^{-6}$ mol·m^{-3} was considered at the gas-liquid interface. Null H$_2$ concentration was considered at the top of the computational domain.

3. Results and discussion

3.1. Bubble growth

The experimental curves, and the growth law applicable to bubble growth in this system have been discussed in detail in a previous publication [15]. In brief, the bubbles growing at the center of the ring electrode have been shown to transition from pressure-driven growth, to diffusion-limited growth, and finally to reaction-limited (also referred to as supply-limited) growth for $R_b > R_e$; where R_e is the mean electrode radius. In other words, the value of the exponent α, the exponent in the bubble growth law $R_b = \beta t_b^\alpha$, decreases from 1 at the start of electrolysis to 1/2 during the diffusion-limited phase, and to 1/3 when the bubble begins to eclipse the electrode.

The results from the simulation were processed identically to the experimental results to ensure comparability. A key limitation in our experimental setup is that, when imaged from the top, bubbles smaller than the pit radius are indistinguishable from the pit itself. This limitation is mimicked by our model where the radius of the simulated bubbles are taken to be the maximum of the r-coordinate along the bubble interface at any given instance in
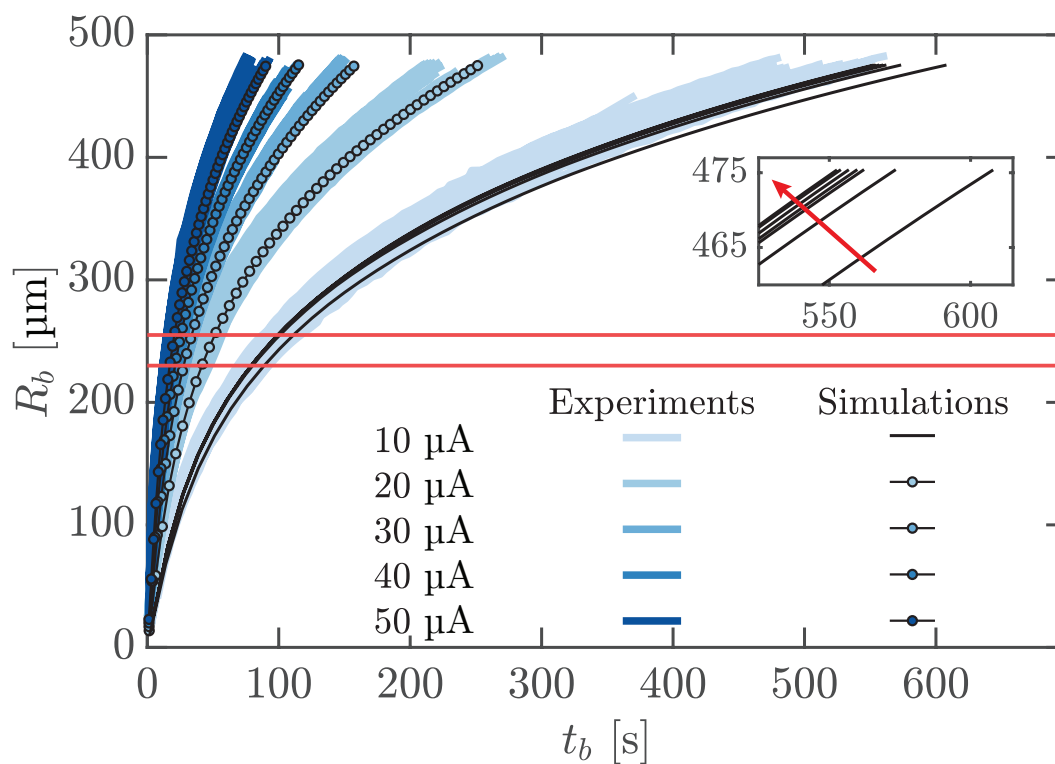
14

Figure 3: Bubble radius R_b of both experimental and simulated bubbles plotted against bubble lifetime t_b. The experimental curves from Raman et al. [15] (blue lines) represent data from 332 bubbles spread across 25 experiments driven by five currents (see legend). The growth curves of a single simulated bubble driven by the four higher currents (20 µA to 50 µA) are shown as circles connected by lines (note that the circles on the simulated curves are undersampled for better readability). The growth curves for 7 successive simulated bubbles driven by 10 µA are plotted as black lines. The inset shows the a zoom-in of growth curves of the seven bubbles driven by 10 µA just before departure. The growth curves for the second to seventh bubbles lie close to one another but are distinct from the first bubble. The horizontal red lines show the inner and outer diameters of the ring electrode. The direction of the red arrow in the inset indicates the succession of bubble growth curves.

15

time. In practice, this means that, $R_b < 10$ μm are not simulated. Note that initially, the bubble grows as a spherical cap of a sphere whose true geometric radius is much larger than the pit radius. This spherical radius is not meaningful for the discussion presented here and was therefore not measured in either the experiment, or the models.

Fig. 3 shows R_b from experiments and simulations plotted against the corresponding bubble lifetimes, t_b for different constant applied currents, i. The bubble nucleation time t_0 for the first simulated bubbles was measured by calculating the linear extrapolation whereas, the nucleation times of subsequent bubbles is known precisely. The bubble lifetime, t_b is then calculated as $t - t_0$ where t is experimental, or simulated time. The experimental curves depict the full spread of data, without distinction between successive bubbles from multiple experiments [15].

Fig. 3 also shows that all simulated bubble growth curves lie within the spread of experimental data. Nevertheless, the model under-predicts the growth rate of bubbles compared to the mean (not plotted) of the experimental data spread from experimental observations. The model predicts that the bubbles take 10-20 % longer to reach the departure radius than the mean departure time from experiments. This is particularly visible for $t_b > 400$ s for the first bubble driven by $i = 10$ μA.

To further investigate the source of this deviation, seven successive bubbles driven by an electrolysis current of 10 μA were simulated.The second bubble reaches its departure radius $\sim 6.2\%$ sooner than the first bubble. However, the inset in Fig. 3, shows that the initial transience quickly approaches a steady-state, and the growth curves of successive bubbles are almost identical. For instance, the departure times of the sixth, and the seventh bubbles differ by $\sim 0.25\%$ (see SI Table SI 1 for bubble departure times). Therefore, it is reasonable to attribute this transience to the development of a pseudo-steady concentration field around the electrode. The development, and stabilization of the concentration field is discussed in Sec. 3.4.

Similar start-up transients have been observed in a previous study of successive elec-
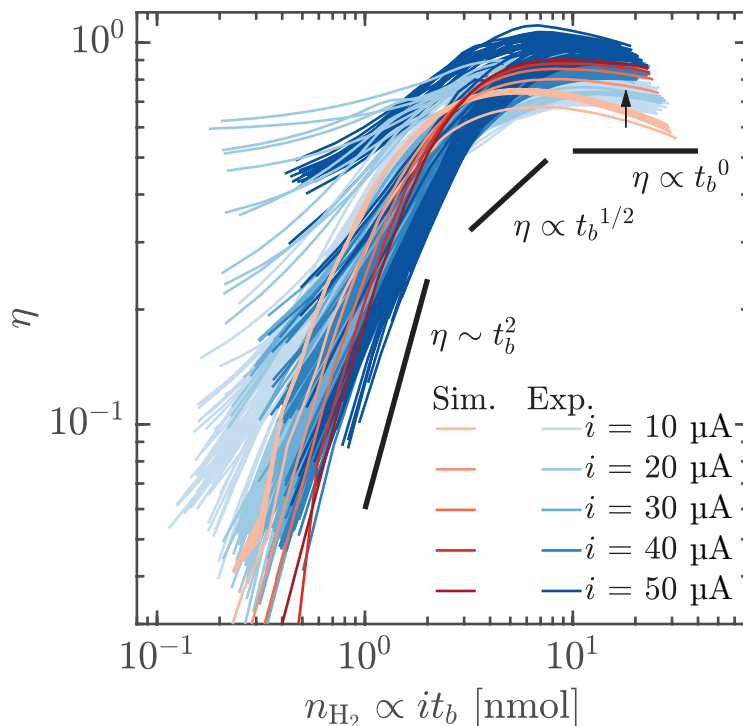
16

Figure 4: Comparison of experimental [15] and simulated instantaneous gas evolution efficiencies for different currents. Instantaneous gas evolution efficiency, η, plotted against the number of moles of hydrogen generated at the electrode at that instant, n_{H_2}. The black arrow indicates curves of the seven successive bubbles driven by 10 µA .

trolytic bubbles [18]. Bubbles in the earlier study grew on electrodes several times larger than their departure radius i.e., $R_b \ll R_e$, with a much lower gas-evolution efficiency (see Eq. 10) and took > 20 min to reach steady-state at current densities up to two orders of magnitude smaller than those considered in this study. Our findings provide a contrasting case where the number of bubble departures required to reach a pseudo-steady concentration field around the electrode is much smaller as a consequence of the bubbles growing to a maximum of $R_b/R_e \simeq 2$. The ring electrode system presented in this study is a closer representation of a unit cell with a single gas bubble on an electrode.

3.2. Instantaneous gas evolution efficiency

From Fig. 3 we learn that the simulated bubbles appear to grow slower than their experimental counterparts in the reaction-limited growth phase i.e., $R_b/R_e > 1$. We explore this further by considering the instantaneous gas evolution efficiency, η which is plotted

17

against n_{H_2}, the number of moles of hydrogen generated at the electrode in Fig. 4. Here, η is defined as:

$$\eta = \frac{\mathrm{d}n_b/\mathrm{d}t_b}{\mathrm{d}n_{H_2}/\mathrm{d}t_b} = \frac{4\pi P_0/3\mathcal{R}T_0}{i/2F}\frac{\mathrm{d}R_b^3}{\mathrm{d}t_b} = \frac{J_b A_b}{i/2F} \tag{10}$$

where, P_0 is the ambient pressure, T_0 is the ambient temperature, $\mathcal{R}$ is the universal gas constant, J_b is the molar flux of H_2 into the bubble, $A_b = 4\pi R_b^2$ is the area of the gas-liquid interface, and F is the Faraday constant. Thus, η is ratio of the rate of uptake of gas by the bubble and the Faradaic rate of generation of gas at the electrode surface . The instantaneous gas evolution efficiency for experimental bubbles was calculated by fitting a smoothing spline and then numerically calculating the derivative dR_b^3/dt_b [15]. Since it is possible to obtain J_b directly from the simulations, the η for the simulated bubbles is directly calculated as the ratio specified on the right hand side of Eq. 10.

The η of both experimental, and simulated bubbles increases with increasing current density. The simulated bubbles also demonstrate the experimentally observed transition from pressure-driven ($\eta \sim t_b^2$) to diffusion-limited ($\eta \sim t_b^{1/2}$), and finally to supply-limited ($\eta \sim t_b^0$) growth. While there is a small decrease in the efficiency of experimental bubbles for the reaction-limited (supply-limited) regime just before departure, η for the simulated bubbles reaches a noticeable maximum before the bubble departure. This is more evident in the case of bubbles driven by 10 μA $n_{H_2} > 4$ nmol or, $\sim t_b > 80$ s. This region of decreasing η before departure coincides with the aforementioned slower bubble growth observed for simulated bubbles in Fig. 3.

The spatial separation of the site of bubble nucleation from the site of electrolysis (the electrode surface) has interesting implications for the time evolution of η, and the concentration field around the bubble. Since the bubble does not grow directly on the electrode surface, there is a finite diffusive flux of H_2 from the electrode towards the bulk electrolyte. Thus, the bubble effectively experiences only a fraction of the total Faradaic flux out of the surface of the electrode. The evolution of η seen in Fig. 4 describes the fraction of the flux at the electrode which drives bubble growth at a given instant. This fraction is determined

18

by the geometry of the system at a given time, which is characterized by R_b/R_e. In the diffusive-growth regime, R_b/R_e is a measure of the distance the gas has to diffuse before reaching the gas-liquid interface. Initially, when the bubble is small and the diffusion path length between the electrode and the bubble interface is large, η is very low. As the bubble grows, this distance decreases; resulting in an increased η.

Once the threshold $R_b/R_e > 1$ is reached, and the bubble transitions to supply-limited growth, the diffusion path length is small and does not appreciably vary further. Diffusion is no longer the limiting factor, and the bubble is expected to grow at a constant volumetric rate. However, as noted earlier, we observe that the η in fact reaches a maxima in this phase of bubble growth. During the early stages of bubble growth when η is low, a majority of the H_2 produced at the electrode diffuses into the electrolyte in the vicinity of the electrode. The emergence of the maxima in η seen in Fig. 4 can be explained by the re-absorption of some of the H_2 that previously diffused into the electrolyte.

Previous studies have shown that bubbles growing atop a carpet of microbubbles, grow with 100 % gas evolution efficiency in a reaction-limited regime when $R_b > R_e$ [20]. In contrast, bubbles in our system exhibit $\eta < 1$ despite growing at a constant volumetric rate indicating that the bubble does not capture all of the H_2 produced at the electrode surface. We explore the reasons for this in the next section by considering the concentration profile of dissolved hydrogen in the vicinity of the bubble.

3.3. Flux along the bubble surface

The spatio-temporal evolution of the flux of H_2 along the bubble surface was evaluated using the model, and Fig. 5 shows the Lagrangian multiplier of the concentration of H_2, c_{lm}, which represents the line integral of the flux of H_2 along the circumference of the bubble surface at a given height. This integral is normalized by the Faradaic flux, and plotted against the non-dimensionalized bubble height z/z_{max}, at different non-dimensionalized bubble lifetimes t_b/t_d. Here, z_{max} is the height of the bubble at a given time, and t_d is the time at which the bubble departs from the pit. From Fig. 5, we make four key observations that
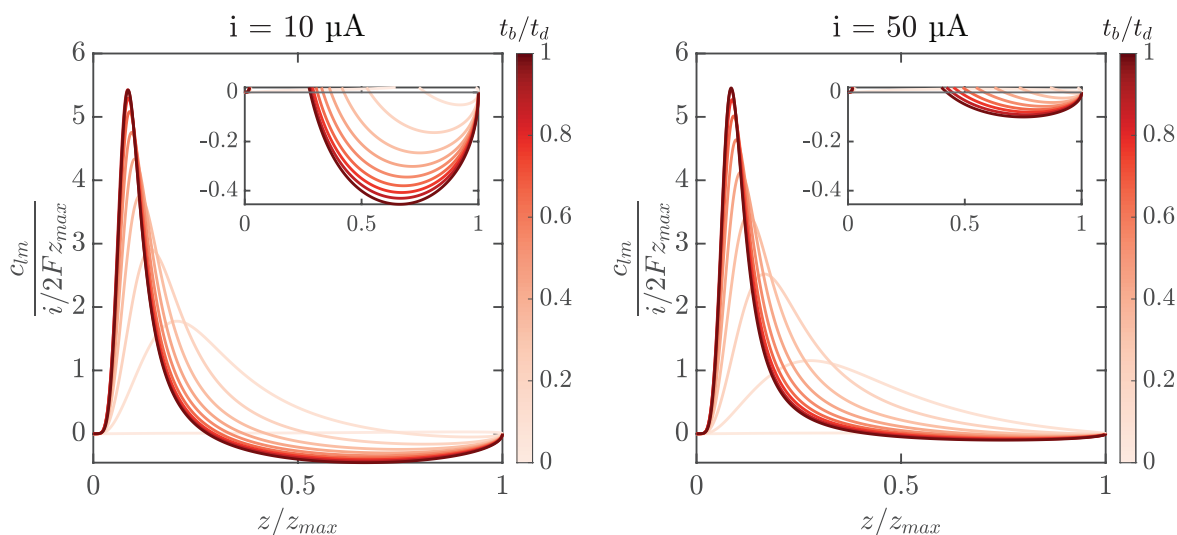
19

Figure 5: The local flux at points along the bubble interface is normalized by the Faradaic flux at the electrode $i/2FA_e$ and plotted as a function of fractional height z_i/z_{max} at different normalized times t_b/t_d (see colorbar) at the lowest (left panel, 10 μA), and the highest (right panel, 50 μA)currents considered in the study. c_{lm} is the Lagrangian multiplier of concentration, and represents the line integral of flux along the surface of the bubble at a given height. The x-axis extends from the bottom of the bubble where it is pinned to the pit ($z/z_{max} = 0$) to the apex of the bubble ($z/z_{max} = 1$). The zoom-ins (insets) show that flux turns negative across a section of the bubble's surface.
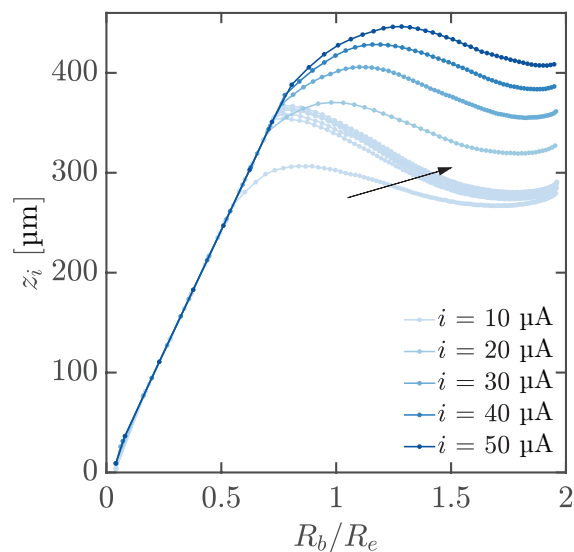

Figure 6: The variation of the flux inversion height i.e., the height along the bubble surface at which the gas diffuses from the bubble to the liquid, is plotted as a function of the non-dimensionalized bubble radius R_b/R_e. The direction of the arrow indicates the order of curves associated with successive bubbles driven by 10 μA from first to seventh.

20

shed further light on the evolution of η discussed in Sec. 3.2.

Firstly, the total molar rate of transport of H_2 into the bubble, which is the area under the curves in Fig. 5, increases with time. This agrees well with transition of the bubble from the diffusion-limited regime to the supply-limited growth regime (discussed in Sec. 3.1 and Sec. 3.3).

Secondly, a peak in the flux curves increases in magnitude, and shifts towards the base of the bubble as it grows larger, and transitions to supply-limited growth. This indicates that the bulk of the flux into the bubble is concentrated near the base of the bubble close to the electrode surface. This has been previously reported as direct-injection, and is characteristic of supply-limited bubble growth [20, 21, 73].

Thirdly, there is a simultaneous outward diffusive flux of hydrogen from the apex of the bubble even as the bubble absorbs hydrogen at the bottom. The outward diffusive flux is visible as the negative portion of the curves in Fig. 5. The magnitude of this outward flux increases with increasing bubble radius. The portion of the bubble's total interfacial area from which hydrogen escapes into the electrolyte also increases with increasing R_b. The re-dissolution of hydrogen from the top of the bubble, contributes to the slight decline in η seen in Fig. 4, just before bubble departure.

Finally, the magnitude of the H_2 outward flux decreases with increasing i. This explains why the η curves of bubbles driven by an electrolysis current of 10 μA in Fig. 4 show a prominent maxima. This also explains why bubbles driven by higher currents are more efficient at gas uptake.

Fig. 6 shows the flux inversion height z_i as a function of the non-dimensionalized bubble radius R_b/R_e for different currents. We define z_i as the height along the bubble surface where the direction of the local flux of hydrogen changes sign, or equivalent to the height of the bubble if no inversion happens. Initially, z_i varies linearly with R_b/R_e, and is $\sim R_b$. This indicates that the bubble is fully immersed in a region of the electrolyte which is saturated with hydrogen gas. Moreover, we note that apex hydrogen loss begins at a greater bubble

21

radius, and at a greater height for higher currents. This happens because, higher electrolysis currents saturate the electrolyte in the vicinity of the bubble, faster. Additionally, successive bubbles driven by 10 µA also show hydrogen re-dissolution at greater heights, and radii. This is because the departure of previous bubbles induces a convective wake which saturates the electrolyte directly above the incipient bubble. Finally, the onset of apex hydrogen re-dissolution coincides with the transition to reaction-limited growth - both of which begin around $R_b = R_e$.

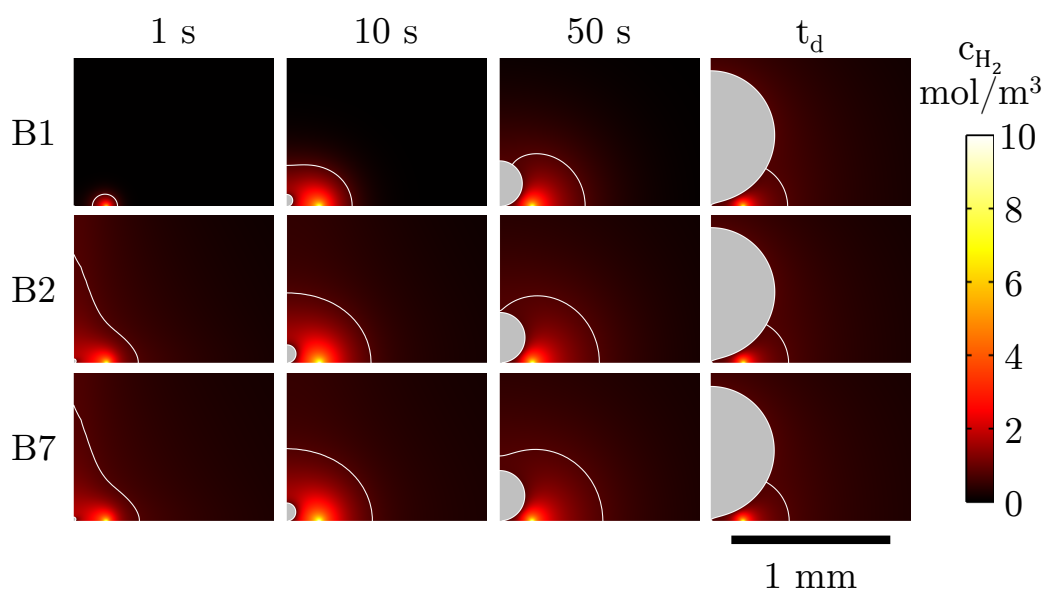## 3.4. Evolution of concentration profiles

Figure 7: The development of the concentration of dissolved hydrogen (see common colorbar) around successive electrolytic bubbles driven by a current of 10 µA is shown at different times - 1 s, 10 s, 50 s, and at t_d when the bubble reaches its departure radius. There is a marked difference between the concentration fields surrounding the first, and the second bubbles (rows B_1 and B_2, respectively). These differences are less remarkable between the second, and the seventh successive bubble (rows B_2 and B_7). Each panel has a white contour line representing the saturation boundary where $c_{H_2} = c_s$. Furthermore, the concentration field surrounding all three bubbles at t_d is similar.

Figure 7 shows the evolution of the concentration of dissolved hydrogen around a bubble driven by an electrolysis current of 10 µA. The concentration of dissolved hydrogen in the electrolyte near the electrode increases right at the start of electrolysis. Thereafter, a diffusive front is formed which grows until it reaches the superhydrophobic cavity at the

22

center of the ring electrode. In the absence of bubble nucleation, this diffusive front will continue to expand. However, the nucleation of the bubble consumes dissolved gas from the supersaturated electrolyte. At its maximum extent, the saturated region extends up to ≈ 350 μm from the substrate; beyond which the electrolyte remains undersaturated throughout the lifetime of the bubble. Initially, the bubbles are fully contained within the saturated region (indicated by white contours in Fig. 7) and therefore, after a short pressure-driven growth regime, exhibit diffusion-limited growth. As the bubble grows by diffusively absorbing hydrogen from the surrounding electrolyte, the bubble interface advances faster than the layer of saturated electrolyte. As a result, the top portion of the bubble is exposed to undersaturated electrolyte and the hydrogen in the bubble begins to re-dissolve at the bubble's apex.
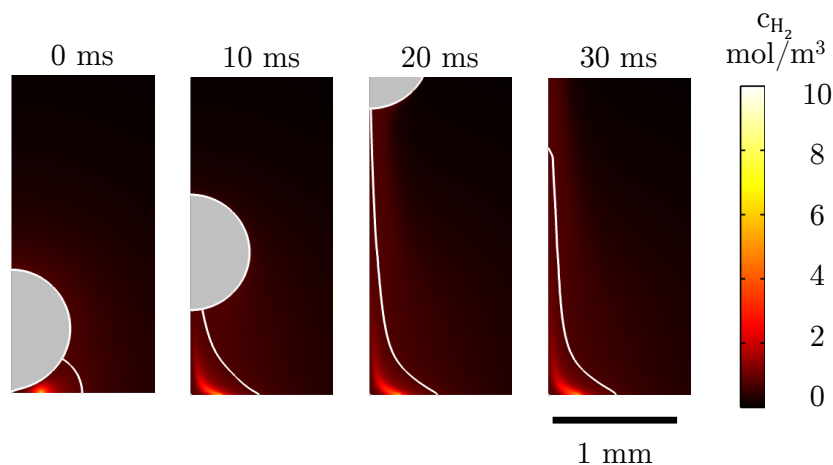

Figure 8: The departure and rise of the first bubble driven driven by 10 μA is shown at 10 ms intervals after bubble departure. The generation of an advective wake, and the subsequent disruption of the concentration profile is visible. The white contour line denotes the extent of the saturation boundary where $c_{H_2} = c_s$.

Fig. 8 shows the departure of the first bubble generates a wake which disrupts the saturated region, and drags it upwards as the bubble rises. This can also be seen in Fig. 7 in the panels corresponding to 1 s after the nucleation of the third and seventh bubbles where the saturation contours extend upwards (left-most panels on rows B3 and B7). Departure-induced advection leads to the development of a pseudo-steady concentration profile. Suc-

cessive bubbles remain within the elongated saturated region for a greater duration, and thus exhibit faster growth (see inset Fig. 3), and greater η (see Fig. 4). It is worth noting that the concentration field surrounding all the bubbles just before departure is almost identical. This indicates that the influence of the departure of the preceding bubble on the growth of the subsequent one is limited to the elongation of the saturation boundary in the initial stages of growth $R_b/R_e < 1$.

4. Conclusions and outlook

We have simulated the growth, and departure of electrolytic bubbles at different currents using a DNS approach. Our study considered the growth, and departure of successive electrolytic bubbles in a spatially decoupled system where the bubbles nucleation on a superhydrophobic pit at the center of a ring electrode where the gas is generated. Moreover, the study considers larger bubbles than previously reported in the literature. These bubbles are shown to outgrow the concentration boundary layer which partly explains the rich bubble growth dynamics. A time-dependent investigation considering coupled fluid flow and mass transfer is presented, which represents a significant advancement regarding the study of Peñas et al. [14]. Finally, the use of an ALE moving mesh topology for the electrolytic bubbles and the use of an interface cutting protocol to handle topology changes during bubble departure are enable the precise calculation of gas flux along the bubble interface.

The simulated bubble growth curves show good agreement with experimental data. The bubbles transition from pressure-driven, to diffusion-limited, to reaction-limited growth. It was observed that the model predicted slower growth for the first bubble driven by the lowest current (10 μA) than seen in experiments. In order to further understand the reason for this, seven successive bubble growth and departures driven by 10 μA were simulated. It was observed that the time evolution of bubble radii of successive bubbles fell within the spread of experimental data indicating the presence of a start-up transience. The convection induced by the departure of successive bubbles was shown to aid the development of a pseudo-steady

24

concentration profile, and the attenuation of the start-up transience.

Three key observations are made in both the experiments, and the model. First, the bubbles exhibit reaction-limited growth with $\eta < 1$, where η is the instantaneous gas evolution efficiency. Second, η reaches a maxima, and decreases in the reaction-limited regime, just before bubble departure. Third, the η of bubbles in the reaction-limited regime increases with increasing current. The underlying reasons for these three observations were explored through the simulations which provided access to spatio-temporal information about the flux of H_2, and the concentration field around the bubble. These data, which are challenging to measure in-situ, show that the three aforementioned observations are caused by the combination of: (i) the separation of the site of nucleation site from the site of electrolysis, and (ii) the diffusive flux of H_2 from the apex of the bubble into the electrolyte.

These two effects appear more pronounced in the model than in the experiments. Furthermore, no appreciable start-up transience was visible in the experiments even at the lowest current. One plausible explanation is that the electrolyte may not have been entirely quiescent during experiments. Relatively weak flows in the electrolyte could alter the concentration field around the bubble. For instance, taking a diffusion length scale equivalent to the mean electrode radius $R_e = 242.5$ µm, a flow velocity > 20 µm/s would imply that the Peclet number $Pe > 1$, and that advection is the dominant phenomena.

The extent of the saturated region provides a natural limit for the departure size of electrolytic bubbles with optimal gas uptake characteristics i.e., high η. We have shown that bubbles that outgrow the saturated region, exhibit a gas evolution efficiency $\eta < 1$ despite growing in a reaction-limited regime. Forced convection of the electrolyte over the electrode is expected to change the size of the saturated zone significantly. Furthermore, the region of saturated electrolyte surrounding several bubbles growing in close proximity are expected to overlap - leading to more intricate mass transfer dynamics. This scenario is further complicated by bubble coalescence. Future studies focusing on these effects are required to fully understand, and optimize the gas evolution efficiency of electrolytic bubbles.

25

Declaration of Competing Interests

The authors declare that they have no known competing financial interests or personal relationships that could have appeared to influence the work reported in this paper.

Credit authorship contribution statement

A.R., Conceptualization, Data Curation, Formal Analysis, Investigation, Methodology, Project administration, Software, Visualization, Writing – original draft, Writing – review & editing. C.C.d.S.P, Software, Writing – review & editing.

H.G., Funding acquisition, Project administration, Supervision, Writing – review & editing.

C.S., Funding acquisition, Methodology, Software, Writing – review & editing.

D.F.R., Funding acquisition, Project administration, Resources, Supervision, Writing – review & editing.

N.P., Funding acquisition, Investigation, Methodology, Software, Validation, Writing – original draft, Writing – review & editing.

Acknowledgements

Supplementary information

Supplemental information can be found in online version, at dx.doi.org/xx.xxx.xxxx.

References

[1] International Energy Agency, The Future of Hydrogen, Technical Report, IEA, IEA, Paris, 2021.

[2] B. R. Alamri, A. R. Alamri, Technical review of energy storage technologies when integrated with intermittent renewable energy, in: 2009 Int. Conf. Sustain. Power Gener. Supply, 2009, pp. 1–5. doi:`10.1109/SUPERGEN.2009.5348055`.

[3] P. Moriarty, D. Honnery, Intermittent renewable energy: The only future source of hydrogen?, International Journal of Hydrogen Energy 32 (2007) 1616–1624. doi:`10.1016/j.ijhydene.2006.12.008`.

[4] International Energy Agency, Net Zero by 2050, Technical Report, IEA, IEA, Paris, 2021.

[5] A. Angulo, P. van der Linde, H. Gardeniers, M. Modestino, D. Fernández Rivas, Influence of Bubbles on the Energy Conversion Efficiency of Electrochemical Reactors, Joule 4 (2020) 555–579. doi:`10.1016/j.joule.2020.01.005`.

[6] A. E. Angulo, D. Frey, M. A. Modestino, Understanding Bubble-Induced Overpotential Losses in Multiphase Flow Electrochemical Reactors, Energy Fuels (2022). doi:`10.1021/acs.energyfuels.2c01543`.

[7] J. Dukovic, Tobias, Charles, The Influence of Attached Bubbles on Potential Drop and Current Distribution at Gas-Evolving Electrodes, J. Electrochem. Soc. 134 (1987) 331. doi:`10.1149/1.2100456`.

[8] J. A. Leistra, P. J. Sides, Hyperpolarization at gas evolving electrodes—II. Hall/heroult electrolysis, Electrochimica Acta 33 (1988) 1761–1766. doi:`10.1016/0013-4686(88)85011-4`.

[9] H. Vogt, R. Balzer, The bubble coverage of gas-evolving electrodes in stagnant electrolytes, Electrochimica Acta 50 (2005) 2073–2079. doi:`10.1016/j.electacta.2004.09.025`.

[10] H. Vogt, The incremental ohmic resistance caused by bubbles adhering to an electrode, J Appl Electrochem 13 (1983) 87–88. doi:`10.1007/BF00615891`.

[11] H. Vogt, The Concentration Overpotential of Gas Evolving Electrodes as a Multiple Problem of Mass Transfer, J. Electrochem. Soc. 137 (1990) 1179. doi:`10.1149/1.2086624`.

[12] H. Vogt, K. Stephan, Local microprocesses at gas-evolving electrodes and their influence on mass transfer, Electrochimica Acta 155 (2015) 348–356. doi:`10.1016/j.electacta.2015.01.008`.

[13] J. A. Leistra, Voltage Components at Gas Evolving Electrodes, J. Electrochem. Soc. 134 (1987) 2442. doi:`10.1149/1.2100218`.

[14] P. Peñas, P. van der Linde, W. Vijselaar, D. van der Meer, D. Lohse, J. Huskens, H. Gardeniers, M. A. Modestino, D. F. Rivas, Decoupling Gas Evolution from Water-Splitting Electrodes, J. Electrochem. Soc. 166 (2019) H769–H776. doi:`10.1149/2.1381914jes`.

[15] A. Raman, P. Peñas, D. van der Meer, D. Lohse, H. Gardeniers, D. Fernández Rivas, Potential response of single successive constant-current-driven electrolytic hydrogen bubbles spatially separated from the electrode, Electrochimica Acta 425 (2022) 140691. doi:`10.1016/j.electacta.2022.140691`.

[16] N. Pande, G. Mul, D. Lohse, B. Mei, Correlating the Short-Time Current Response of a Hydrogen Evolving Nickel Electrode to Bubble Growth, J. Electrochem. Soc. 166 (2019) E280–E285. doi:`10.1149/2.0191910jes`.

[17] G. F. Swiegers, R. N. L. Terrett, G. Tsekouras, T. Tsuzuki, R. J. Pace, R. Stranger, The prospects of developing a highly energy-efficient water electrolyser by eliminating or mitigating bubble effects, Sustainable Energy Fuels 5 (2021) 1280–1310. doi:`10.1039/D0SE01886D`.

[18] P. van der Linde, P. Peñas-López, Á. Moreno Soto, D. van der Meer, D. Lohse, H. Gardeniers, D. Fernández Rivas, Gas bubble evolution on microstructured silicon substrates, Energy Environ. Sci. 11 (2018) 3452–3462. doi:`10.1039/C8EE02657B`.

[19] P. van der Linde, Á. Moreno Soto, P. Peñas-López, J. Rodríguez-Rodríguez, D. Lohse, H. Gardeniers, D. van der Meer, D. Fernández Rivas, Electrolysis-Driven and Pressure-Controlled Diffusive Growth of Successive Bubbles on Microstructured Surfaces, Langmuir 33 (2017) 12873–12886. doi:`10.1021/acs.langmuir.7b02978`.

[20] X. Yang, F. Karnbach, M. Uhlemann, S. Odenbach, K. Eckert, Dynamics of Single Hydrogen Bubbles at a Platinum Microelectrode, Langmuir 31 (2015) 8184–8193. doi:`10.1021/acs.langmuir.5b01825`.

[21] N. P. Brandon, G. H. Kelsall, Growth kinetics of bubbles electrogenerated at microelectrodes, J Appl Electrochem 15 (1985) 475–484. doi:`10.1007/BF01059288`.

[22] L. E. Scriven, On the dynamics of phase growth, Chemical Engineering Science 10 (1959) 1–13. doi:`10.1016/0009-2509(59)80019-1`.

[23] G. Sakuma, Y. Fukunaka, H. Matsushima, Nucleation and growth of electrolytic gas bubbles under microgravity, International Journal of Hydrogen Energy 39 (2014) 7638–7645. doi:10.1016/j.ijhydene.2014.03.059.

[24] D. E. Westerheide, J. W. Westwater, Isothermal growth of hydrogen bubbles during electrolysis, AIChE J. 7 (1961) 357–362. doi:10.1002/aic.690070303.

[25] P. Lv, P. Peñas, H. Le The, J. Eijkel, A. van den Berg, X. Zhang, D. Lohse, Self-Propelled Detachment upon Coalescence of Surface Bubbles, Phys. Rev. Lett. 127 (2021) 235501. doi:10.1103/PhysRevLett.127.235501.

[26] J. Chen, L. Guo, X. Hu, Z. Cao, Y. Wang, Dynamics of single bubble departure from TiO2 nanorod-array photoelectrode, Electrochimica Acta 274 (2018) 57–66. doi:10.1016/j.electacta.2018.04.051.

[27] R. Iwata, L. Zhang, K. L. Wilke, S. Gong, M. He, B. M. Gallant, E. N. Wang, Bubble growth and departure modes on wettable/non-wettable porous foams in alkaline water splitting, Joule 5 (2021) 887–900. doi:10.1016/j.joule.2021.02.015.

[28] J. Li, S. Gong, L. Zhang, P. Cheng, X. Ma, F. Hong, Wetting States and Departure Diameters of Bubbles on Micro-/Nanostructured Surfaces, Langmuir 38 (2022) 3180–3188. doi:10.1021/acs.langmuir.1c03212.

[29] H. Vogt, The problem of the departure diameter of bubbles at gas-evolving electrodes, Electrochimica Acta 34 (1989) 1429–1432. doi:10.1016/0013-4686(89)87183-X.

[30] R. Yan, R. Pham, C.-L. Chen, Activating Bubble's Escape, Coalescence, and Departure under an Electric Field Effect, Langmuir 36 (2020) 15558–15571. doi:10.1021/acs.langmuir.0c02903.

[31] S. R. German, M. A. Edwards, H. Ren, H. S. White, Critical Nuclei Size, Rate, and Activation Energy of H2 Gas Nucleation, J. Am. Chem. Soc. 140 (2018) 4047–4053. doi:10.1021/jacs.7b13457.

[32] Á. M. Soto, S. R. German, H. Ren, D. van der Meer, D. Lohse, M. A. Edwards, H. S. White, The Nucleation Rate of Single O_2 Nanobubbles at Pt Nanoelectrodes, Langmuir 34 (2018) 7309–7318. doi:3.

[33] D. Lohse, Bubble puzzles: From fundamentals to applications, Phys. Rev. Fluids 3 (2018) 110504. doi:10.1103/PhysRevFluids.3.110504.

[34] C. Gabrielli, F. Huet, M. Keddam, P. Rousseau, V. Vivier, Scanning Electrochemical Microscopy for Investigating Gas Bubble/Liquid Interfaces, Electrochem. Solid-State Lett. 6 (2003) E23. doi:10.1149/1.1604971.

[35] Y. Liu, C. Jin, Y. Liu, K. H. Ruiz, H. Ren, Y. Fan, H. S. White, Q. Chen, Visualization and Quantification of Electrochemical H2 Bubble Nucleation at Pt, Au, and MoS2 Substrates, ACS Sens. 6 (2021) 355–363. doi:10.1021/acssensors.0c00913.

[36] Y. Liu, X. Lu, Y. Peng, Q. Chen, Electrochemical Visualization of Gas Bubbles on Superaerophobic Electrodes Using Scanning Electrochemical Cell Microscopy, Anal. Chem. 93 (2021) 12337–12345. doi:`10.1021/acs.analchem.1c02099`.

[37] Y. Wang, E. Gordon, H. Ren, Mapping the Nucleation of H_2 Bubbles on Polycrystalline Pt via Scanning Electrochemical Cell Microscopy, J. Phys. Chem. Lett. 10 (2019) 3887–3892. doi:`10.1021/acs.jpclett.9b01414`.

[38] N. Pande, S. K. Chandrasekar, D. Lohse, G. Mul, J. A. Wood, B. T. Mei, D. Krug, Electrochemically Induced pH Change: Time-Resolved Confocal Fluorescence Microscopy Measurements and Comparison with Numerical Model, J. Phys. Chem. Lett. 11 (2020) 7042–7048. doi:`10.1021/acs.jpclett.0c01575`.

[39] A. J. Leenheer, H. A. Atwater, Imaging Water-Splitting Electrocatalysts with pH-Sensing Confocal Fluorescence Microscopy, J. Electrochem. Soc. 159 (2012) H752–H757. doi:1.

[40] J. Bleeker, A. P. Kahn, L. M. Baumgartner, F. C. Grozema, D. A. Vermaas, W. F. Jager, Quinolinium-Based Fluorescent Probes for Dynamic pH Monitoring in Aqueous Media at High pH Using Fluorescence Lifetime Imaging, ACS Sens. (2023). doi:`10.1021/acssensors.3c00316`.

[41] K. J. Vachaparambil, K. E. Einarsrud, Numerical simulation of bubble growth in a supersaturated solution, Applied Mathematical Modelling 81 (2020) 690–710. doi:`10.1016/j.apm.2020.01.017`.

[42] K. J. Vachaparambil, K. E. Einarsrud, Numerical simulation of continuum scale electrochemical hydrogen bubble evolution, Applied Mathematical Modelling 98 (2021) 343–377. doi:`10.1016/j.apm.2021.05.007`.

[43] H. Liu, L.-m. Pan, J. Wen, Numerical simulation of hydrogen bubble growth at an electrode surface, Can. J. Chem. Eng. 94 (2016) 192–199. doi:`10.1002/cjce.22378`.

[44] S. Zhan, R. Yuan, Y. Huang, W. Zhang, B. Li, Z. Wang, J. Wang, Numerical simulation of hydrogen bubble growth and mass transfer on horizontal microelectrode surface under electrode-normal magnetic field, Physics of Fluids 34 (2022) 112120. doi:`10.1063/5.0127299`.

[45] A. Taqieddin, R. Nazari, L. Rajic, A. Alshawabkeh, Review—Physicochemical Hydrodynamics of Gas Bubbles in Two Phase Electrochemical Systems, J. Electrochem. Soc. 164 (2017) E448. doi:`10.1149/2.1161713jes`.

[46] D. Gueyffier, J. Li, A. Nadim, R. Scardovelli, S. Zaleski, Volume-of-Fluid Interface Tracking with Smoothed Surface Stress Methods for Three-Dimensional Flows, Journal of Computational Physics 152 (1999) 423–456. doi:`10.1006/jcph.1998.6168`.

[47] D. Lörstad, L. Fuchs, High-order surface tension VOF-model for 3D bubble flows with high density ratio, Journal of Computational Physics 200 (2004) 153–176. doi:`10.1016/j.jcp.2004.04.001`.

[48] M. Sussman, P. Smereka, S. Osher, A Level Set Approach for Computing Solutions to Incompressible Two-Phase Flow, Journal of Computational Physics 114 (1994) 146–159. doi:`10.1006/jcph.1994.1155`.

[49] H.-Z. Yuan, C. Shu, Y. Wang, S. Shu, A simple mass-conserved level set method for simulation of multiphase flows, Phys. Fluids 30 (2018) 040908. doi:`10.1063/1.5010152`.

[50] K. J. Vachaparambil, Interface Resolved Simulations of Continuum Scale Electrochemical Hydrogen Evolution, Ph.D. thesis, NTNU, 2020.

[51] F. Khalighi, N. G. Deen, Y. Tang, A. W. Vreman, Hydrogen bubble growth in alkaline water electrolysis: An immersed boundary simulation study, Chemical Engineering Science 267 (2023) 118280. doi:`10.1016/j.ces.2022.118280`.

[52] F. Sepahi, N. Pande, K. L. Chong, G. Mul, R. Verzicco, D. Lohse, B. T. Mei, D. Krug, The effect of buoyancy driven convection on the growth and dissolution of bubbles on electrodes, Electrochimica Acta 403 (2022) 139616. doi:`10.1016/j.electacta.2021.139616`.

[53] X. Yang, D. Baczyzmalski, C. Cierpka, G. Mutschke, K. Eckert, Marangoni convection at electrogenerated hydrogen bubbles, Phys. Chem. Chem. Phys. 20 (2018) 11542–11548. doi:`10.1039/C8CP01050A`.

[54] A. M. Meulenbroek, A. W. Vreman, N. G. Deen, Competing Marangoni effects form a stagnant cap on the interface of a hydrogen bubble attached to a microelectrode, Electrochimica Acta 385 (2021) 138298. doi:`10.1016/j.electacta.2021.138298`.

[55] J. Massing, G. Mutschke, D. Baczyzmalski, S. S. Hossain, X. Yang, K. Eckert, C. Cierpka, Thermocapillary convection during hydrogen evolution at microelectrodes, Electrochimica Acta 297 (2019) 929–940. doi:`10.1016/j.electacta.2018.11.187`.

[56] R. Hreiz, L. Abdelouahed, D. Fünfschilling, F. Lapicque, Electrogenerated bubbles induced convection in narrow vertical cells: PIV measurements and Euler–Lagrange CFD simulation, Chemical Engineering Science 134 (2015) 138–152. doi:`10.1016/j.ces.2015.04.041`.

[57] A. Zarghami, N. G. Deen, A. W. Vreman, CFD modeling of multiphase flow in an alkaline water electrolyzer, Chemical Engineering Science 227 (2020) 115926. doi:`10.1016/j.ces.2020.115926`.

[58] F. F. Rivera, T. Pérez, L. F. Castañeda, J. L. Nava, Mathematical modeling and simulation of electrochemical reactors: A critical review, Chemical Engineering Science 239 (2021) 116622. doi:`10.1016/j.ces.2021.116622`.

[59] W. A. El-Askary, I. M. Sakr, K. A. Ibrahim, A. Balabel, Hydrodynamics characteristics of hydrogen evolution process through electrolysis: Numerical and experimental studies, Energy 90 (2015) 722–737. doi:`10.1016/j.energy.2015.07.108`.

[60] G. Wosiak, J. da Silva, S. S. Sena, R. N. de Andrade, E. Pereira, CFD simulation and experimental comparison of bubble-induced convection during electrochemical water splitting, Chemical Engineering Journal 433 (2022) 133194. doi:`10.1016/j.cej.2021.133194`.

[61] L. F. Catañeda, F. F. Rivera, T. Pérez, J. L. Nava, Mathematical modeling and simulation of the reaction environment in electrochemical reactors, Current Opinion in Electrochemistry 16 (2019) 75–82. doi:`10.1016/j.coelec.2019.04.025`.

[62] K. Stewart, L. Lair, B. De La Torre, N. L. Phan, R. Das, D. Gonzalez, R. C. Lo, Y. Yang, Modeling and Optimization of an Alkaline Water Electrolysis for Hydrogen Production, in: 2021 IEEE Green Energy Smart Syst. Conf. IGESSC, IEEE, Long Beach, CA, USA, 2021, pp. 1–6. doi:`10.1109/IGESSC53124.2021.9618679`.

[63] A. Taqieddin, M. R. Allshouse, A. N. Alshawabkeh, Editors' Choice—Critical Review—Mathematical Formulations of Electrochemically Gas-Evolving Systems, J. Electrochem. Soc. 165 (2018) E694. doi:`10.1149/2.0791813jes`.

[64] P. T. H. M. Verhallen, L. J. P. Oomen, A. J. J. M. v. d. Elsen, J. Kruger, J. M. H. Fortuin, The diffusion coefficients of helium, hydrogen, oxygen and nitrogen in water determined from the permeability of a stagnant liquid layer in the quasi-s, Chemical Engineering Science 39 (1984) 1535–1541. doi:`10.1016/0009-2509(84)80082-2`.

[65] R. Sander, Compilation of Henry's law constants (version 4.0) for water as solvent, Atmospheric Chem. Phys. 15 (2015) 4399–4981. doi:`10.5194/acp-15-4399-2015`.

[66] I. Grombik, J. Lasa, I. Šliwka, P. Mochalski, J. Pusz, M. Jackowicz-Korczynski, New method of measuring hydrogen concentration in air, Environ. Prot. Eng. (2006).

[67] P. R. Amestoy, I. S. Duff, J.-Y. L'Excellent, J. Koster, A Fully Asynchronous Multifrontal Solver Using Distributed Dynamic Scheduling, SIAM J. Matrix Anal. Appl. 23 (2001) 15–41. doi:`10.1137/S0895479899358194`.

[68] P. R. Amestoy, A. Guermouche, J.-Y. L'Excellent, S. Pralet, Hybrid scheduling for the parallel solution of linear systems, Parallel Computing 32 (2006) 136–156. doi:`10.1016/j.parco.2005.07.004`.

[69] U. M. Ascher, L. R. Petzold, Computer Methods for Ordinary Differential Equations and Differential-Algebraic Equations, SIAM, 1998.

[70] R. Jafari, T. Okutucu-Özyurt, 3D numerical modeling of boiling in a microchannel by arbitrary Lagrangian–Eulerian (ALE) method, Applied Mathematics and Computation 272 (2016) 593–603. doi:`10.1016/j.amc.2015.03.042`.

[71] J. Donea, A. Huerta, J.-P. Ponthot, A. Rodríguez-Ferran, Arbitrary Lagrangian–Eulerian Methods, in: Encyclopedia of Computational Mechanics, John Wiley & Sons, Ltd, 2004, pp. 414–437. doi:`10.1002/0470091355.ecm009`.

[72] G. Anjos, N. Mangiavacchi, N. Borhani, J. R. Thome, 3D ALE Finite-Element Method for Two-Phase Flows With Phase Change, Heat Transf. Eng. 35 (2014) 537–547. doi:`10.1080/01457632.2013.833407`.

[73] J. Qin, T. Xie, D. Zhou, L. Luo, Z. Zhang, Z. Shang, J. Li, L. Mohapatra, J. Yu, H. Xu, X. Sun, Kinetic study of electrochemically produced hydrogen bubbles on Pt electrodes with tailored geometries, Nano Res. (2021). doi:`10.1007/s12274-020-3132-y`.

33